# 3D printable low density B2+BCC refractory element based complex concentrated alloy with excellent balance of mechanical properties

Advika Chesetti, Sucharita Banerjee, Sriswaroop Dasari, Mohan Sai Kiran Nartu, S.M. Varahabhatla, Abhishek Sharma, Abhishek Ramakrishnan, Daniel Satko, Stephane Gorsse, Ayman Salem, et al.

# 3D printable low density B2+BCC refractory element based complex concentrated alloy with excellent balance of mechanical properties

Advika Chesetti [a,b], Sucharita Banerjee [b,c], Sriswaroop Dasari [a], Mohan Sai Kiran Nartu [a,b], S.M. Varahabhatla [a,b], Abhishek Sharma [a], Abhishek Ramakrishnan [d], Daniel Satko [d], Stephane Gorsse [e], Ayman Salem [d], Rajarshi Banerjee [a,b,*]

[a] Department of Materials Science & Engineering, University of North Texas, Denton, TX 76207, United States

[b] Center for Agile and Adaptive Additive Manufacturing, University of North Texas, Denton, TX 76207, United States

[c] Department of Mechanical Engineering, The University of Texas at Austin, Austin, TX 78712, United States

[d] MRL Materials Resources LLC, 123 Fairground Rd. Twp, Xenia, OH 45385, United States

[e] University Bordeaux, CNRS, Bordeaux INP, ICMCB, UMR 5026, Pessac 33600, France

*Corresponding author: raj.banerjee@unt.edu

## Abstract

While complex concentrated alloys (CCAs), involving a large fraction of refractory elements, are promising candidates for structural applications, their relatively high densities, processing challenges, and low plasticity, has retarded their development. Here, we report a 3D printable low-density precipitation strengthened CCA of composition, $Al_{10}Nb_{15}Ta_5Ti_{30}Zr_{40}$. The chemical homogeneity in the alloy deposited using laser bed powder fusion process is substantially better as compared to the as-cast ingot. This homogeneity is attributed to the enhanced solubility at the high temperatures experienced during laser melting, small melt pool dimensions, and the high cooling rates. The as-built CCA exhibited an excellent balance of room temperature mechanical properties, a compressive yield stress ~1400 MPa, peak stress ~1700 MPa, and plastic strain exceeding 45%. These properties can be attributed to its unique as-processed microstructure consisting of refined grains incorporating a high density of sub-grain boundaries, containing a nanoscale two-phase mixture of an ordered B2 and disordered BCC solid solution phases.

**Keywords**

Refractory high entropy alloys; laser additive manufacturing; laser powder bed fusion**;** microstructure; mechanical properties.

## Introduction

CCAs, also referred to a high entropy alloys (HEAs), when they are single phase, are based on the concept of combining several elements in equi-atomic amounts to develop materials which exhibit desirable properties [1]. Furthermore, to develop materials for high temperature applications, CCAs based on refractory elements have been developed [2]. Such CCAs have also been referred to as refractory HEAs or RHEAs in the literature. Some RHEAs have been found to exhibit two phases which include B2 and BCC phases showing close resemblance to Ni-based superalloys [3–8]. Additionally, these CCAs show superior mechanical properties at elevated temperatures but exhibit poor ductility at room temperature. The poor ductility of these RHEAs has been attributed to the B2 phase therefore creating an interest for a deeper understanding of the mechanical properties of this phase. Previously, the B2 phase of low-density CCA ($Al_{0.25}$NbTaTiZr) was investigated by identifying the composition of the B2 phase through atom probe tomography (APT)[5,6,9,10]. Subsequently the identified B2 composition, which was found to be 10Al-15Nb-5Ta-30Ti-40Zr (at%), was melted separately to form a new CCA. Furthermore, this new composition exhibited relatively high compressive ductility and strength at room temperature[10].

Conventional processing of refractory element based CCAs via the vacuum arc melting route is challenging owing to the high melting points of the principal alloying elements, as well as a marked difference in the melting temperatures amongst some of the constituent refractory elements [11]. Refractory alloys are known to be difficult to process given their affinity for oxygen and limited plasticity. Additionally, the slow cooling rates involved in the process give sufficient time for the elements to segregate during solidification leading to compositionally inhomogeneous ingots with dendritic microstructure [12]. Couzinié et al. [13] observed coarse Nb- and Ta-rich dendrites separated by segregated Ti, Zr, Hf-rich inter-dendritic zones in regions of the arc-melted TiZrHfNbTa that experienced slow cooling. However, no elemental segregation and dendritic microstructures were observed in the rapidly solidified zone. This type of microstructure was also found in numerous studies [14–17] where the dendrites were enriched in high melting point

elements, while the inter-dendritic regions were enriched in low melting point elements, solidifying at the end. Although, chemically homogeneous ingots have been fabricated using arc melting, they are often accompanied by multiple re-melting runs making the process strenuous. For instance, Yang et al. [12] fabricated equimolar HfMoNbTaTi RHEA by arc melting with 12 melting procedures to achieve chemical homogeneity. This makes Additive Manufacturing (AM) a more desirable processing technique given the rapid cooling rates encountered in the procedure. Li et al. [18] observed dendrites with an average size of 4 μm in laser cladded $W_xNbMoTa$, whereas Zhang et al. [19] found the primary and secondary dendritic arm spacings to be ~ 6.59 μm and ~ 1.68 μm on average respectively in laser powder bed fusion (LPBF) deposited NbMoTaW RHEA as opposed to the 20 μm arm spacing in the as-cast counterpart.

Additive Manufacturing is an appealing alternative as very high temperatures can be quickly reached to melt the refractories due to the laser or electron beam sources. The fabrication of complex geometries is also made easier, resulting in more design and manufacturing freedom in the fabrication of refractory element based CCAs for complex structural parts. Furthermore, the availability of several powder-feeders in some AM systems gives more control over the alloy composition [20–23]. The process, however, comes with its own set of challenges. AM is constrained by the energy absorption capacity of the powders, along with the size and shape of the particles that impact their flowability and the fraction of them being carried into the melt pool [24]. However, these issues can be minimized by optimizing laser parameters and scan strategies [25]. For instance, Dobbelstein et al. [26] developed a crack-free graded $Ti_{25}Zr_{50-x}Nb_xTa_{25}$ CCA by utilizing an in-situ low laser power deposition step followed by a high laser power re-melting step. Therefore, it is of interest to utilize AM to fabricate chemically homogeneous and crack-free CCAs.

While relatively low strength refractory alloys and CCAs involving these elements, have been successfully deposited using AM techniques, fabrication of defect-free high strength refractory element based CCAs still pose a challenge. In the current study, a low density $Al_{10}Nb_{15}Ta_5Ti_{30}Zr_{40}$ alloy was identified to be a potential candidate for LPBF processing due to its high plasticity reported in the as-cast and homogenized form [27,28]. The AM processability and evolution of microstructure of this refractory based CCA have been assessed in this study, along with the impact on its mechanical properties in contrast to the conventionally processed counterpart.

## Materials and Methods

A cube of dimensions 14.28 mm x 9.58 mm x 7.14 mm with the composition $Al_{10}Nb_{15}Ta_5Ti_{30}Zr_{40}$ was deposited using LPBF technique using a feedstock of pre-alloyed powders. Test cubes of $Al_{10}Nb_{15}Ta_5Ti_{30}Zr_{40}$ alloy were additive manufactured using a 3D systems PROX200 (California, U.S.); LPBF system. Process parameter optimization of builds with laser power, scanning speed, hatch spacing and layer thickness of 230 W, 900 mm/s, 62 μm and 30 μm, respectively, revealed no cracks prior to removal from the build plate with successful deposition and a density of 6.448 g/cm$^3$. The composition of the deposit was found to be $Al_{11.4}Nb_{14}Ta_{3.5}Ti_{34}Zr_{37.1}$ (at%) based on SEM-EDS and $Al_{11.5}Nb_{13}Ta_{3.5}Ti_{31}Zr_{41}$ (at%) using atom probe tomography (APT). The primary microstructural characterization of these samples was carried out using a FEG-SEM (FEI Nova NanoSEM 230). Compositional analysis was carried out using an energy dispersive spectrometer (EDS) attached to SEM (Model: Apollo X, EDAX LLC, Mahwah, New Jersey). X-Ray Diffraction was carried out using the Rigaku Ultima III XRD under CuKα radiation (1.54 Å) at 0.05°/min with a step size of 0.025°. The MDI Jade software was using to analyze the XRD data. For transmission electron microscopy (TEM) of these samples, lamellae were prepared using a dual-beam focused ion beam milling system (FEI Nova 200 Nanolab FIB/SEM). Detailed transmission electron microscopy (TEM) for these lamellae was carried out in FEI Tecnai G2 F20 ST TEM capable of operating in both scanning and transmission modes and equipped with an EDS detector (EDAX LLC, Mahwah, New Jersey). Compositional analysis of the samples was carried out using atom probe tomography (APT). The specimen tips for the same were prepared using a dual-beam FIB (FEI Nova 200 Nanolab FIB/SEM). The APT was operated in laser mode with the specimen's base temperature at 30 K, pulse rate of 200 kHz, pulse energy of 50 nJ, and a target detection rate of 5-10 ions detected every 1000 pulses. Data analysis was performed using the software package AP Suite 6.1.

Mechanical properties were estimated via quasi-static compression tests on 4.25×4.25 mm square cross-section samples with 6.8 mm height (height to width ratio ~1.6) using an MTS© servo-hydraulic universal testing machine (UTM). Both top and bottom surfaces of the samples were polished to a 600-grit finish prior to the tests and Teflon film (~50 μm) was used as lubrication

between the sample surface and the compression platens. All the tests were conducted at a strain rate of $1\times10^{-3}$ $s^{-1}$.

**Results and Discussion**

The phases present in the as-built RHEA were initially investigated using XRD. The diffractogram in Fig. 1(a) shows the presence of two phases which can be consistently indexed as BCC1 and BCC2. The lattice parameters of these phases are 340.3 pm and 342.1 pm respectively. The lattice misfit calculated with respect to BCC1 is ~0.5%, which indicates the possibility of a coherent or semi-coherent interface between these phases. Fig. 1(b-c) show low and high magnification backscattered SEM micrographs respectively, with the build direction from bottom to top. While Fig. 1(b) shows the fine grain size and many semi-circular melt pool boundaries, some level of compositional partitioning can be discerned in Fig. 1(c) along the melt pool boundaries. The crystallographic and the compositional homogeneity were further investigated using EBSD and EDS. Fig. 1(d) shows the inverse pole figure (IPF) map from the as-built sample. The grain average diameter determined from grain area-based calculations is ~98 μm. Fig. 1(e) showing the [001], [011], and [111] BCC pole figure plots, indicates a random texture along the build direction.

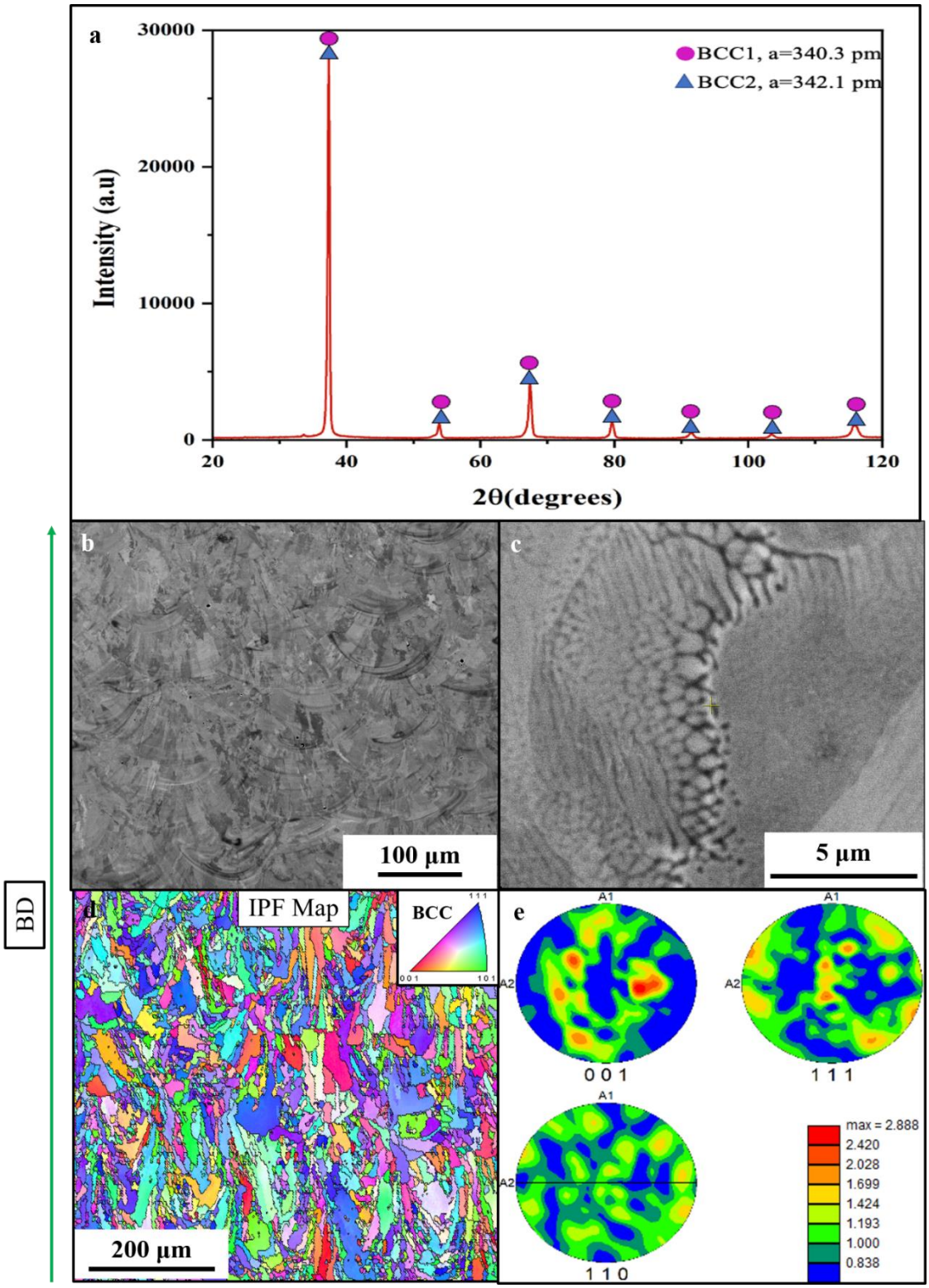


**Figure 1:** (a) X-ray diffraction pattern of as-built $Al_{10}Nb_{15}Ta_5Ti_{30}Zr_{40}$ showing two BCC based phases. Backscattered SEM images at (b) low magnification showing overall microstructure and (c) at high magnification showing compositional partitioning near melt-pool boundaries. (d) Inverse Pole Figure (IPF) and (e) texture plots showing random texture.

The comparison of chemical homogeneity in as-built and conventionally cast microstructures is shown in Fig. 2. Figs. 2(a,b) shows the backscattered SEM micrographs from both samples. It must be noted that the scale of the microstructures is very different between the two micrographs. Additionally, Fig. 2(a) shows a region near melt pool boundary of the as-built RHEA that appeared to have the most compositional heterogeneity. The Al and Zr K-α images from each condition are shown on Figs. (c-f). These images illustrate that the as-deposited microstructure is far more homogenous than the as-cast counterpart.

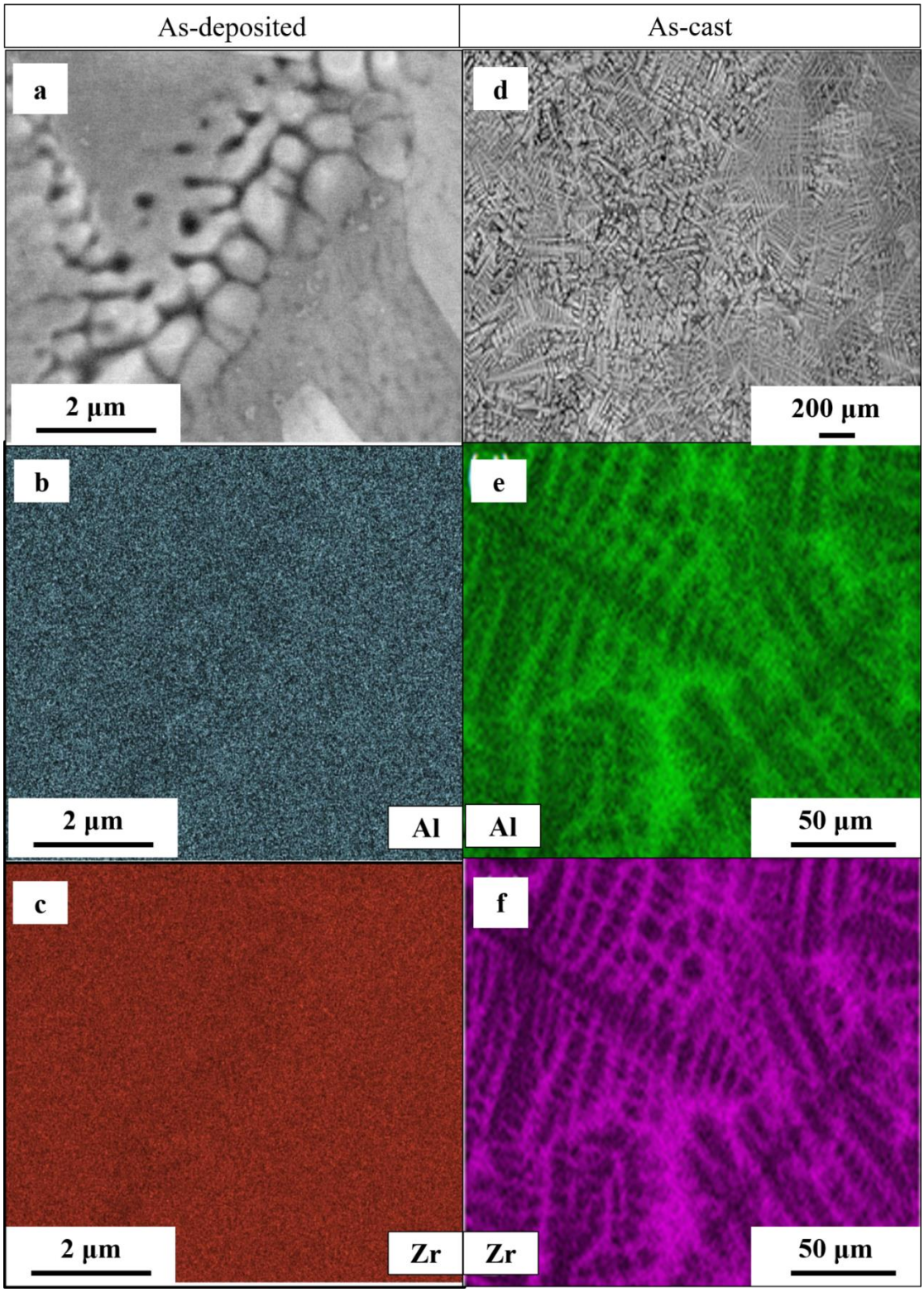


**Figure 2:** (a) SEM backscattered image of the as-built $Al_{10}Nb_{15}Ta_5Ti_{30}Zr_{40}$. (b-c) Compositional mapping of (b) Al, and (c) Zr in the as-built condition. (d) SEM backscattered image of the as-cast (AC) $Al_{10}Nb_{15}Ta_5Ti_{30}Zr_{40}$. (e-f) Compositional mapping of (e) Al, and (f) Zr in the AC condition.

The striking difference between as-cast and as-built alloy (Fig. 2) shows the potential of LPBF techniques in obtaining chemically homogenous material thereby eliminating or reducing the cost of homogenization treatments. The very high temperatures reached during laser melting, high cooling rates and the subsequent heating and cooling cycles minimized the compositional partitioning during solidification. However, this may not be the case for all refractory alloys because sufficient thermodynamic driving force (highly negative or positive enthalpy of mixing) for partitioning may assist segregation [14–17,29]. In the current alloy, $Al_{10}Nb_{15}Ta_5Ti_{30}Zr_{40}$, Ti and Zr (both group IV elements) which are completely miscible form the majority ~70 at.%. Nb and Ta are also miscible in Ti and Zr at high temperatures. The role of Al is difficult to assess but the current study shows that Al does not enhance partitioning tendency, albeit leads to the formation of coherent B2 ordered domains, which will be discussed later.

The compression properties of this alloy, $Al_{10}Nb_{15}Ta_5Ti_{30}Zr_{40}$ in the as-cast and homogenized condition were reported previously [27,28]. The compressive stress-strain curve of this alloy in as-built condition is shown in Fig. 3(a). Both engineering and true stress-strain curves were shown in this figure for comparison. The as-deposited material exhibited a yield stress of 1390 MPa, flow stress of 1685 MPa and a plasticity of 45%. The strain hardening observed in this as-deposited $Al_{10}Nb_{15}Ta_5Ti_{30}Zr_{40}$ is comparable to some of the best RHEAs reported so far [30,31]. Fig. 3(b) shows an Ashby plot between specific yield stress and strain in compression for RHEAs exhibiting single-phase and dual-phase microstructures. This plot reveals that our $Al_{10}Nb_{15}Ta_5Ti_{30}Zr_{40}$ alloy in as-built condition stands out amongst many RHEAs reported in literature [32–34]. While the as-cast and homogenized $Al_{10}Nb_{15}Ta_5Ti_{30}Zr_{40}$ alloy did not fail during compression testing up to 60% plastic strain, the yield stress was only ~1000 MPa. In comparison, the LPBF as-built RHEA exhibited a substantially higher yield stress with slightly less plasticity. The reasons for the superior properties of as-built $Al_{10}Nb_{15}Ta_5Ti_{30}Zr_{40}$ were investigated employing high magnification EBSD, TEM and APT.

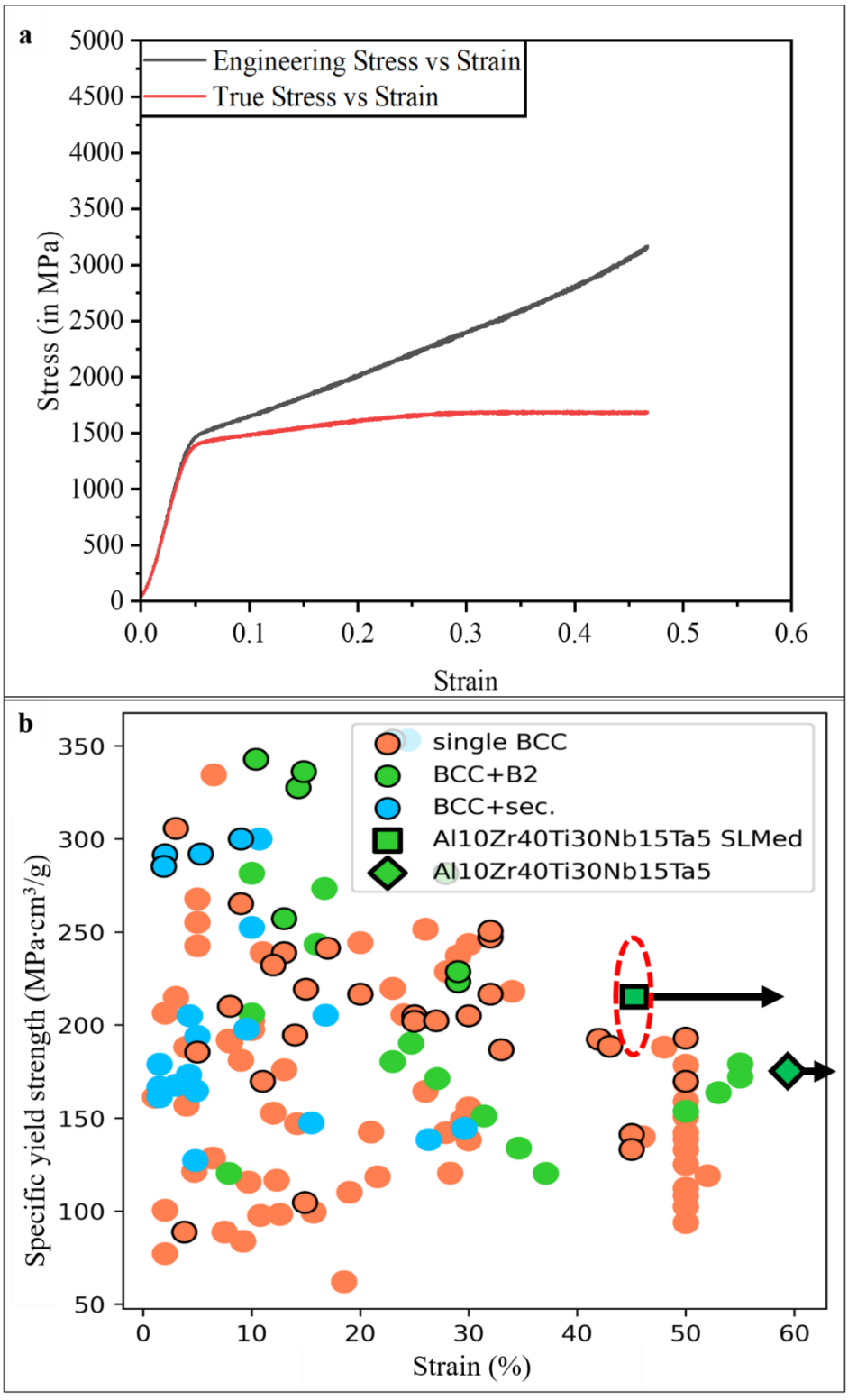


**Figure 3:** (a) Compressive engineering and true stress-strain plots for as-built RHEA (b) Comparison of specific yield strength vs strain (%) values for various RHEAs.

Fig. 4 shows the high magnification EBSD results from the as-built $Al_{10}Nb_{15}Ta_5Ti_{30}Zr_{40}$ sample. The IPF map is shown in Fig. 4(a) and the grain boundary map is shown in Fig. 4(b). The formation of sub-grains and many low angle boundaries (1 to 15$^o$ misorientation) or LABs can be observed from these figures. Further, one of the grains in Fig. 4(a) is highlighted in Figs. 4(c-d) which show fine-scale sub-grains and a network of LABs within them. Such a fine and complex grain boundary structure is expected to have significantly contributed to the yield stress, especially since the Hall-Petch coefficient or grain boundary strengthening coefficient 'K' has been reported to be quite high in case of HEAs [35].

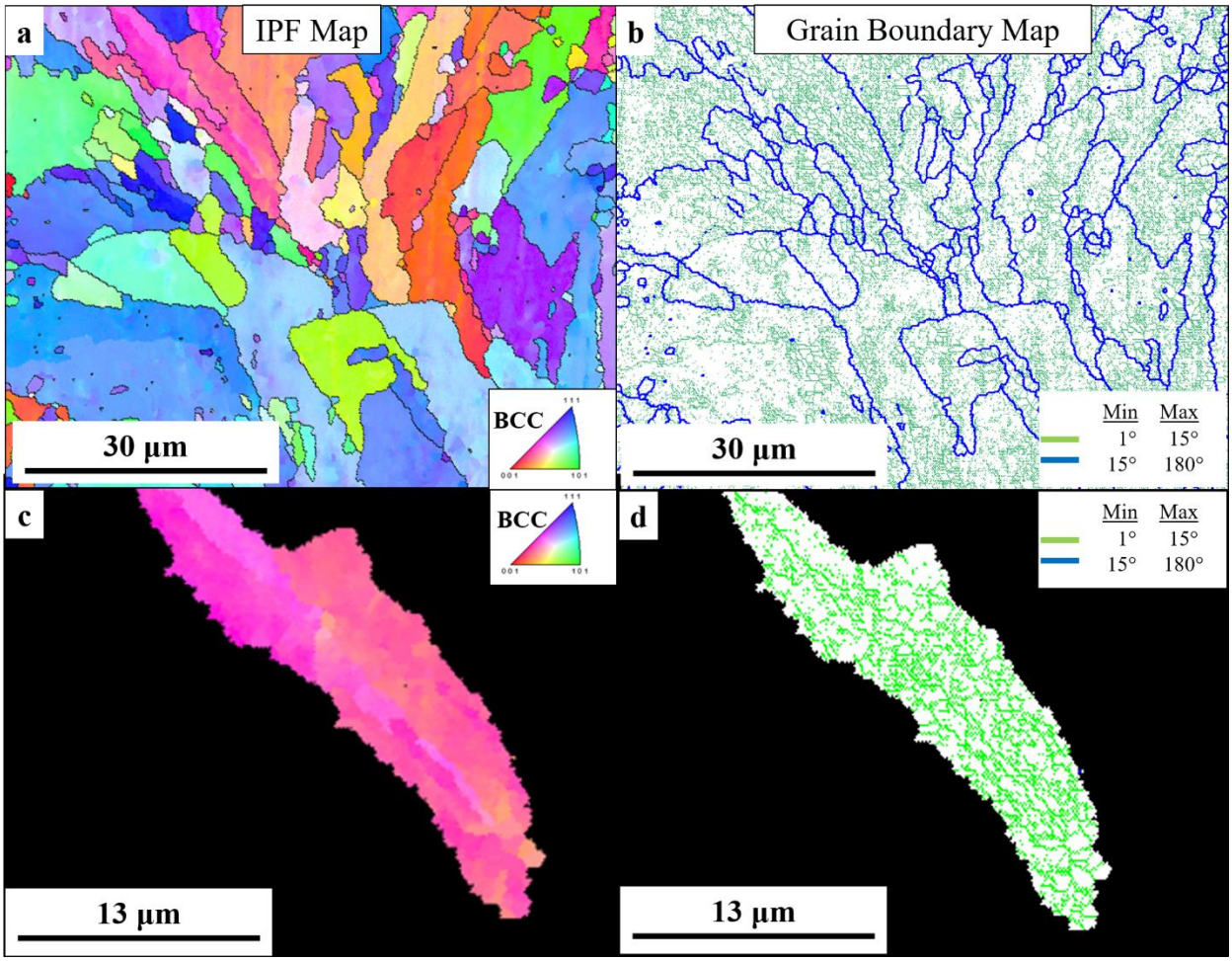


**Figure 4:** (a) Inverse Pole Figure (IPF), and (b) grain boundary map obtained from EBSD. (c) High magnification IPF, and (d) grain boundary map of one of the grains in (a) highlighting numerous low angle grain boundaries (LABs) within the grain.

In addition to grain boundary strengthening, $Al_{10}Nb_{15}Ta_5Ti_{30}Zr_{40}$ alloy in its as-built condition is also strengthened by a mixture of ordered and disordered phases at nanoscale, as revealed by TEM

and APT. Fig. 5(a) shows the selected area electron diffraction pattern (SAEDP) recorded near [001] BCC zone axis. This diffraction pattern shows that in addition to the disordered BCC reflections (fundamental), superlattice reflections at {001} positions indicative of B2 ordering are present in the microstructure. A dark-field micrograph recorded from one of the {001} reflections revealed a speckle contrast suggesting a nanoscale mixture of BCC and B2 phases as reported previously [36]. The presence of both ordered B2 and disordered BCC phases is further substantiated by the HR-TEM image in Fig. 5(c). The interface between BCC and B2 phases in this micrograph is outlined by a red dashed line and indicates a continuous fully coherent BCC lattice between the disordered and ordered phases. The bright field image recorded near [011] BCC zone axis in Fig. 5(d) revealed a significant dislocation density in the as-deposited material. This is presumably due to the heating-cooling cycles during deposition and the thermal contraction stresses during cooling. The compositional partitioning between BCC and B2 phases was further investigated using APT and the results are shown in Figs. 5(e-g).

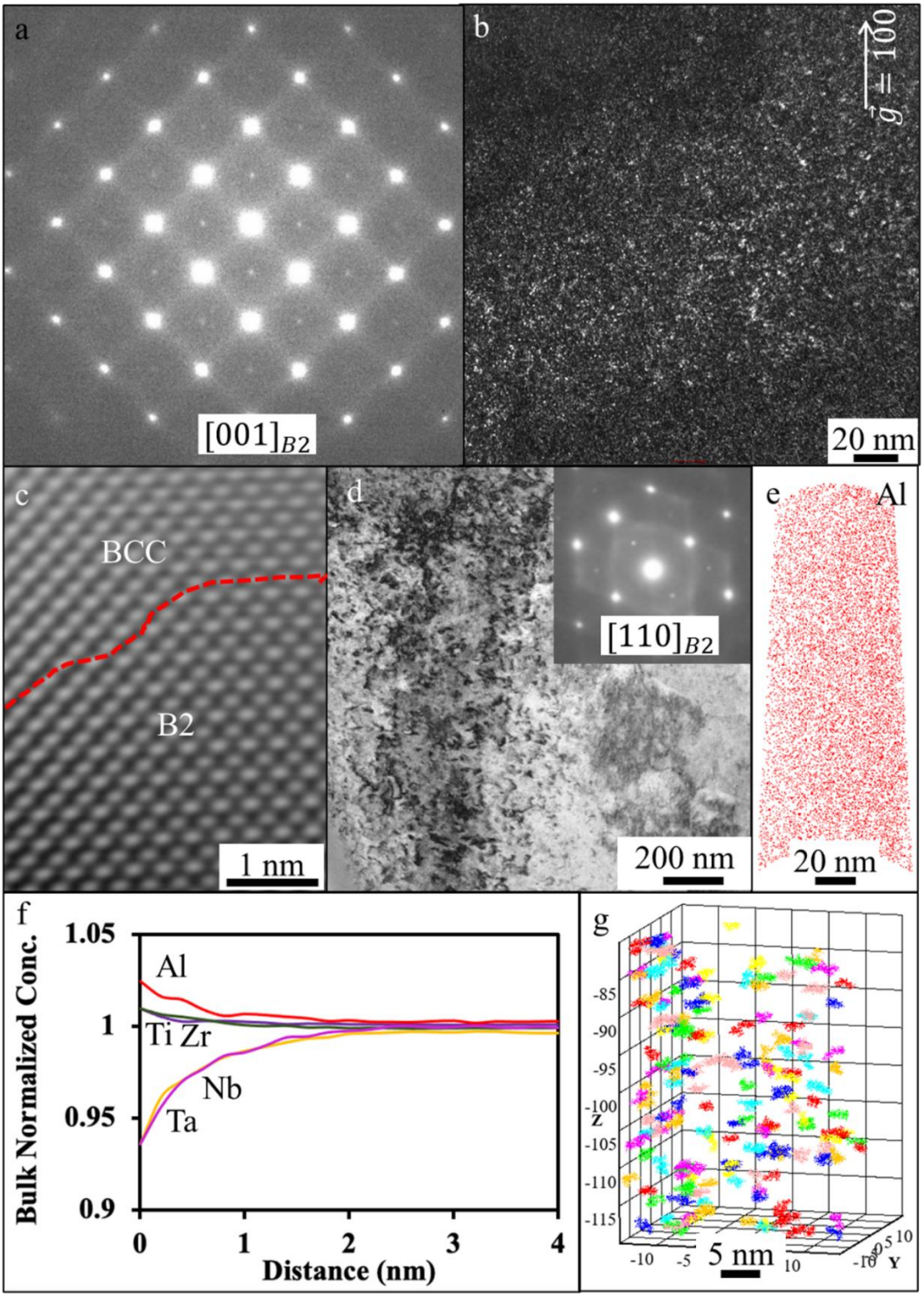


**Figure 5:** (a) TEM diffraction pattern near [001] BCC zone axis showing superlattice reflections indicative of B2 phase. (b) Dark field image from a {001} super-lattice diffraction spot highlighting B2 domains. (c) HR-TEM image showing a BCC/B2 interface. (d) Bright field image showing dislocation density in as-built condition. (e) APT reconstruction of Al ion map, (f) radial distribution function plot about Al center atom, and (g) Al-Ti-Zr rich clusters in a 30 x 30 x 40 $nm^3$ obtained from cluster analysis.

Although the TEM results conclusively established the presence of BCC and B2 phases, the raw Al ion map in Fig. 5(e) did not reveal any obvious chemical partitioning. However, the compositional partitioning tendencies have further been examined using radial distribution functions [37]. Fig. 5(f) shows that if we choose Al, Ti, or Zr as the center atoms, the distribution of concentration of Al, Ti, and Zr is higher than Nb and Ta within a radius of ~2 nm. This strongly indicates a tendency for the clustering between Al, Ti, and Zr atoms, as well as between Nb and Ta atoms. Based on this evidence of non-random distribution of elements, cluster analysis [38,39] was performed to reveal the details of Al, Ti, Zr-rich clusters. The resultant Al-Ti-Zr rich clusters are shown in Fig. 5(g). It was found that these clusters on average contain 13.8% Al, 34.9% Ti, and 44.6% Zr (at.%) as opposed to 10% Al, 30% Ti, and 40% Zr in the bulk. Further, the volume fraction of Al-Ti-Zr rich clusters was found to be 3.5% with an average cluster radius of 1.25 nm. Based on their composition, it can be concluded that these Al-Ti-Zr rich clusters correspond to the ordered B2 regions in the microstructure, while the surrounding Nb-Ta rich regions correspond to the BCC phase. Furthermore, it should be noted that the two different BCC phases BCC1 and BCC2 observed in the XRD patterns, correspond to the ordered B2 and disordered BCC phases in this microstructure.

The strength-plasticity combination of the as-built RHEA under compression was found to be superior to many RHEAs reported in the literature including the same $Al_{10}Nb_{15}Ta_5Ti_{30}Zr_{40}$ alloy in as-cast and homogenized condition (refer to Fig. 3(b)). Detailed microstructural characterization (Figs. 4-5) using EBSD, TEM, and APT revealed that the high strength is primarily due to three contributions, (1) Hall-Petch or grain boundary strengthening including LABs (2) Precipitation strengthening from ordered B2 domains and (3) Strengthening from dislocation density. As a result, the $Al_{10}Nb_{15}Ta_5Ti_{30}Zr_{40}$ alloy exhibited a yield stress ~1400 MPa at room temperature. The as-built alloy exhibited significant strain hardening possibly arising from the ordered B2 domains inhibiting dislocation motion.

## Conclusions

A low density refractory high entropy alloy, consisting of a two-phase mixture consisting of nanoscale ordered B2 and disordered BCC phases, was successfully printed using the laser powder bed fusion technique. The as-built alloy exhibited excellent chemical homogeneity, much better as

compared to the cast ingot. This homogeneity is attributed to the very high temperatures experienced during laser melting and the high cooling rates. More importantly, the constituents of the alloy and their concentrations favor the formation of solid solution at high temperatures due to their solid-state miscibility. The compressive yield strength of the as-printed alloy at room temperature was found to be ~1400 MPa with a plasticity greater 45% (did not fail). Such a high yield strength coupled with the low density of this alloy, makes it superior as compared to many other RHEAs including conventionally processed, cast and homogenized $Al_{10}Nb_{15}Ta_5Ti_{30}Zr_{40}$. The main factors contributing to the yield strength were found to be (1) grain and sub-grain boundaries, (2) B2 precipitation, and (3) dislocation density.

## Acknowledgements

This work was supported by the U.S. Air Force Office of Scientific Research under Grant Nos. FA8649-20-P-0938, FA9550-17-1-0395 and FA9550-21-1-0304. The authors acknowledge the infrastructure and support of Center for Agile & Adaptive and Additive Manufacturing (CAAAM) funded through State of Texas Appropriation #190405-105-805008-220 at the University of North Texas. The authors would also like to acknowledge Materials Research Facility (MRF) for access to advanced characterized techniques.

## Declaration of Interest

None

## References

[1] J.W. Yeh, S.K. Chen, S.J. Lin, J.Y. Gan, T.S. Chin, T.T. Shun, C.H. Tsau, S.Y. Chang, Advanced Engineering Materials 6 (2004) 299–303.
[2] O.N. Senkov, D.B. Miracle, K.J. Chaput, J.P. Couzinie, Journal of Materials Research 33 (2018) 3092–3128.
[3] O.N. Senkov, C. Woodward, D.B. Miracle, JOM 66 (2014) 2030–2042.
[4] O.N. Senkov, D. Isheim, D.N. Seidman, A.L. Pilchak, Entropy 18 (2016).
[5] O.N. Senkov, J.K. Jensen, A.L. Pilchak, D.B. Miracle, H.L. Fraser, Materials and Design 139 (2018) 498–511.
[6] J.K. Jensen, B.A. Welk, R.E.A. Williams, J.M. Sosa, D.E. Huber, O.N. Senkov, G.B. Viswanathan, H.L. Fraser, Scripta Materialia 121 (2016) 1–4.
[7] V. Soni, B. Gwalani, O.N. Senkov, B. Viswanathan, T. Alam, D.B. Miracle, R. Banerjee, Journal of Materials Research 33 (2018) 3235–3246.

[8] V. Soni, O.N. Senkov, B. Gwalani, D.B. Miracle, R. Banerjee, Scientific Reports 8 (2018).
[9] O.N. Senkov, D. Isheim, D.N. Seidman, A.L. Pilchak, Entropy 18 (2016).
[10] V. Soni, O.N. Senkov, J.P. Couzinie, Y. Zheng, B. Gwalani, R. Banerjee, Materialia (Oxf) 9 (2020).
[11] O.N. Senkov, G.B. Wilks, D.B. Miracle, C.P. Chuang, P.K. Liaw, Intermetallics (Barking) 18 (2010) 1758–1765.
[12] C. Yang, H. Bian, K. Aoyagi, Y. Hayasaka, K. Yamanaka, A. Chiba, Materials and Design 212 (2021).
[13] J.P. Couzinié, G. Dirras, L. Perrière, T. Chauveau, E. Leroy, Y. Champion, I. Guillot, Materials Letters 126 (2014) 285–287.
[14] J.P. Couzinié, L. Lilensten, Y. Champion, G. Dirras, L. Perrière, I. Guillot, Materials Science and Engineering A 645 (2015) 255–263.
[15] B. Zhang, M.C. Gao, Y. Zhang, S. Yang, S.M. Guo, Materials Science and Technology (United Kingdom) 31 (2015) 1207–1213.
[16] C.C. Juan, M.H. Tsai, C.W. Tsai, C.M. Lin, W.R. Wang, C.C. Yang, S.K. Chen, S.J. Lin, J.W. Yeh, Intermetallics (Barking) 62 (2015) 76–83.
[17] O.N. Senkov, G.B. Wilks, J.M. Scott, D.B. Miracle, Intermetallics (Barking) 19 (2011) 698–706.
[18] Q. Li, H. Zhang, D. Li, Z. Chen, S. Huang, Z. Lu, H. Yan, Materials 12 (2019).
[19] H. Zhang, Y. Zhao, S. Huang, S. Zhu, F. Wang, D. Li, Materials 12 (2019).
[20] S. Gorsse, C. Hutchinson, M. Gouné, R. Banerjee, Science and Technology of Advanced Materials 18 (2017) 584–610.
[21] J. Kim, A. Wakai, A. Moridi, Journal of Materials Research 35 (2020) 1963–1983.
[22] A. Ostovari Moghaddam, N.A. Shaburova, M.N. Samodurova, A. Abdollahzadeh, E.A. Trofimov, Journal of Materials Science and Technology 77 (2021) 131–162.
[23] M.A. Melia, S.R. Whetten, R. Puckett, M. Jones, M.J. Heiden, N. Argibay, A.B. Kustas, Applied Materials Today 19 (2020).
[24] H. Dobbelstein, E.L. Gurevich, E.P. George, A. Ostendorf, G. Laplanche, Additive Manufacturing 24 (2018) 386–390.
[25] H. Zhang, W. Xu, Y. Xu, Z. Lu, D. Li, International Journal of Advanced Manufacturing Technology 96 (2018) 461–474.
[26] H. Dobbelstein, E.L. Gurevich, E.P. George, A. Ostendorf, G. Laplanche, Additive Manufacturing 25 (2019) 252–262.
[27] V. Soni, O.N. Senkov, J.P. Couzinie, Y. Zheng, B. Gwalani, R. Banerjee, Materialia (Oxf) 9 (2020).
[28] O.N. Senkov, J.P. Couzinie, S.I. Rao, V. Soni, R. Banerjee, Materialia (Oxf) 9 (2020).
[29] M. Widom, Journal of Materials Research 33 (2018) 2881–2898.
[30] O.N. Senkov, J. Gild, T.M. Butler, Journal of Alloys and Compounds 862 (2021).
[31] O.N. Senkov, J.M. Scott, S. v. Senkova, D.B. Miracle, C.F. Woodward, Journal of Alloys and Compounds 509 (2011) 6043–6048.
[32] S. Gorsse, D.B. Miracle, O.N. Senkov, Acta Materialia 135 (2017) 177–187.
[33] C.K.H. Borg, C. Frey, J. Moh, T.M. Pollock, S. Gorsse, D.B. Miracle, O.N. Senkov, B. Meredig, J.E. Saal, Scientific Data 7 (2020).
[34] S. Gorsse, M.H. Nguyen, O.N. Senkov, D.B. Miracle, Data in Brief 21 (2018) 2664–2678.

[35] A. Jagetia, M.S.K.K.Y. Nartu, S. Dasari, A. Sharma, B. Gwalani, R. Banerjee, Materials Research Letters 9 (2021) 213–222.
[36] V. Soni, B. Gwalani, T. Alam, S. Dasari, Y. Zheng, O.N. Senkov, D. Miracle, R. Banerjee, Acta Materialia 185 (2020) 89–97.
[37] F. de Geuser, W. Lefebvre, D. Blavette, Philosophical Magazine Letters 86 (2006) 227–234.
[38] J.M. Hyde, E.A. Marquis, K.B. Wilford, T.J. Williams, Ultramicroscopy 111 (2011) 440–447.
[39] L.T. Stephenson, M.P. Moody, P. v. Liddicoat, S.P. Ringer, in: Microscopy and Microanalysis, 2007, pp. 448–463.